

# Metal-Mediated Nanoscale Cerium Oxide Inactivates Human Coronavirus and Rhinovirus by Surface Disruption

Craig J. Neal, Candace R. Fox, Tamil Selvan Sakthivel, Udit Kumar, Yifei Fu, Christina Drake, Griffith D. Parks, and Sudipta Seal\*



Cite This: <https://doi.org/10.1021/acsnano.1c04142>



Read Online

ACCESS |



Metrics & More



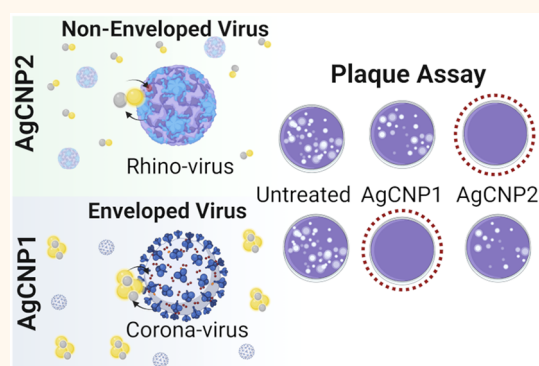
Article Recommendations



Supporting Information

**ABSTRACT:** The COVID19 pandemic has brought global attention to the threat of emerging viruses and to antiviral therapies, in general. In particular, the high transmissibility and infectivity of respiratory viruses have been brought to the general public's attention, along with the need for highly effective antiviral and disinfectant materials/products. This study has developed two distinct silver-modified formulations of redox-active nanoscale cerium oxide (AgCNP1 and AgCNP2). The formulations show specific antiviral activities toward tested OC43 coronavirus and RV14 rhinovirus pathogens, with materials characterization demonstrating a chemically stable character for silver nanophases on ceria particles and significant differences in  $Ce^{3+}/Ce^{4+}$  redox state ratio (25.8 and 53.7%  $Ce^{3+}$  for AgCNP1 & 2, respectively). *In situ* electrochemical studies further highlight differences in formulation-specific viral inactivation and suggest specific modes of action. Altogether, the results from this study support the utility of AgCNP formulations as high stability, high efficacy materials for use against clinically relevant virus species.

**KEYWORDS:** nanoceria, cerium oxide, respiratory virus, coronavirus, antiviral, nanomedicine



The evolving SARS-CoV2 pandemic has led to a surge in fundamental and applied virus-related research. In particular, the high infectivity of the SARS-CoV2 virus, leading to the COVID-19 disease in humans, has inspired substantial research effort into the specific pathology mechanisms and of the specific structure(s) of the virus.<sup>1–3</sup> The pervasive impact of the COVID-19 pandemic has typified the threat of respiratory viruses as highly transmissible and with high rates of infectivity. Such viruses remain a constant threat to human populations, with novel variants emerging annually due to widespread human infection. The specificity of virus interactions makes targeting through pharmaceutical intervention simultaneously more tractable and less practical. As an example, the presence of a glycan shield, a field of glycan moieties on the spike protein surface (coronaviruses), protects binding sites from nonspecific interaction.<sup>4–6</sup> Complex features, such as this, coupled with the growing threat of antibiotic/antimicrobial drug resistance, makes the synthesis of small molecule therapeutics contraindicated.<sup>7,8</sup> Additionally, the growing number of variants emerging makes the value of a high specificity inhibitor species equally problematic.

The use of metal and metal oxide nanomaterials has been studied in various antibacterial/antiviral applications, with a broader basis for pathogen toxicity. Transition metal-based materials have shown exceptional broad-spectrum antibacterial activity as well as antiviral efficacy.<sup>9–11</sup> Further, these formulations are substantially less susceptible to deactivation through physical and chemical conditions as compared to small molecule and biologic agents. In particular, silver has been a staple among such elements in medical and personal products: conferring strong antimicrobial activity. While these materials have seen broad application due to their availability and presence in existing consumer products, their use is still limited by their stability in targeted applications.

**Received:** May 15, 2021

**Accepted:** August 20, 2021

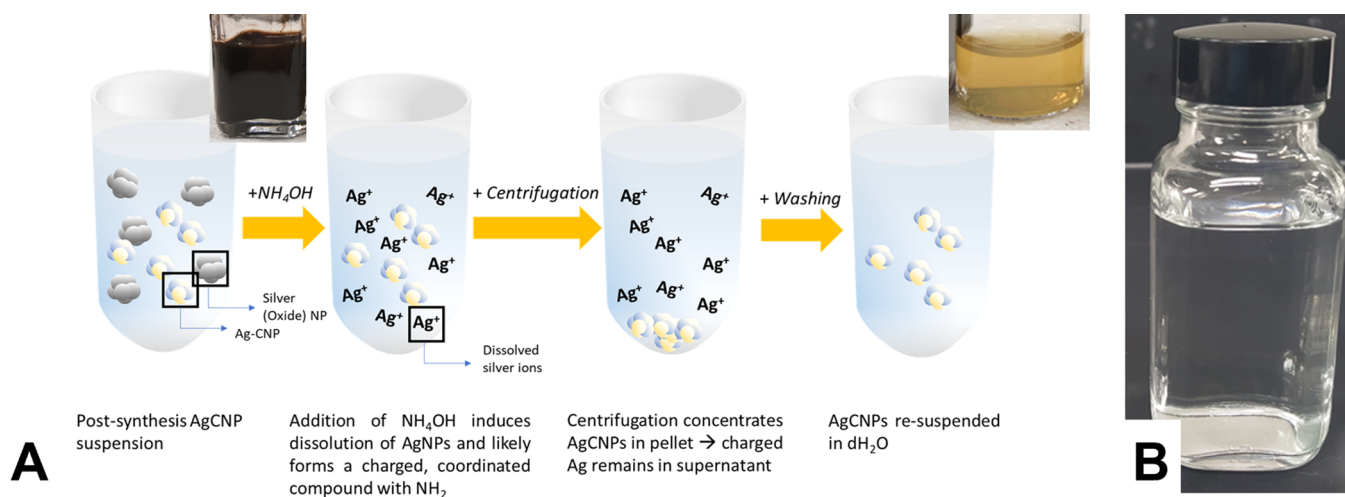


**Figure 1.** Syntheses for AgCNP1 and 2. Formation of AgCNP1 occurs via multiple-step synthesis beginning with a forced hydrolysis and followed by a postsynthesis digestion process (A) to remove secondary silver phases evolved during AgCNP formation. Addition of 1 N  $\text{NH}_4\text{OH}$  postsynthesis leads to selective dissolution of silver phases due to chemical affinity of silver for amine formation (as Tollen's reagent;  $[\text{Ag}(\text{NH}_3)_2]^+$ ). Washing before and after the postsynthesis process removes residual chemical species/reagents. AgCNP2 (B) are formed via the specific reaction chemistry between silver and hydrogen peroxide. At acidic pH's, free solid silver phases undergo oxidation: disfavoring the formation of secondary nanomaterial phases. AgCNP2 is aged, *in situ*, and dialyzed to remove unreacted components. AgCNP1 dispersions are yellow-colored and become turbid at higher concentrations, while AgCNP2 solutions are completely translucent and clear. Visible differences between the formulations are ascribed to the larger particle sizes (greater Mie scattering) in AgCNP1 relative to AgCNP2 (~50 nm v. Twenty nm, respectively, via TEM imaging), and to differences in silver-ceria interface character (AgCNP1: poly crystalline particles of silver and ceria crystallites; AgCNP2: silver-ceria binary particles).

The utility of metallic nanoparticles, such as silver-based materials, arises from their electron transfer reactions, leading to material ionization and decomposition.<sup>12,13</sup> Further, the ionic strength environment and higher temperature can lead to corrosion. Corroding of active materials leads to their inactivation and loss of charge transferability. However, taking cues from catalytic science, metallic nanoparticles may be stabilized by incorporating reducible cerium oxide support structures.

Cerium oxide nanomaterials have shown substantial biomedical efficacy in literature: functioning largely to produce/ameliorate reactive oxygen species through redox cycling (interconversion between  $\text{Ce}^{3+}$  and  $\text{Ce}^{4+}$  states in physiological conditions), oxygen vacancy loss/formation, and interaction with biochemical substrates/ $\text{O}_2$ .<sup>14–17</sup> The related set of chemical reactions produced by nanoscale cerium oxide has been compared to native enzyme behavior and collectively considered enzyme-mimetic activities. For this reason, ceria and other redox-active nanomaterials have been referred to as *nanozymes* or *artificial zymes*.<sup>18</sup> The oxide and reducible (i.e., able to form stable oxygen vacancies) chemical character of ceria permits its function in biocorrosive environments and to stabilize less redox-stable phases, such as biocidal transition metal nanomaterials in harsh catalytic environments.<sup>19–24</sup>

In the presented study, two distinct formulations of silver-modified cerium oxide nanoparticles are produced, characterized, and tested for antiviral efficacy. Microscopy and photoelectron spectroscopy show clear differences in the redox state composition of cerium, the size of formulation particles, and the presentation of silver phases with respect to ceria matrix. Electrochemical and bandgap measurements provide insight into the nature of silver phases along with providing evidence of their stabilization by the cerium oxide phase. Antiviral efficacy was determined for two types of human respiratory viruses (nonenveloped RV14, enveloped OC43), with AgCNP

formulations showing specific antiviral activities. *In situ* electrochemical impedance spectroscopic methods were performed and corroborate the specificity of AgCNP formulation/virus-type interactions over incubation periods. From this data, along with results from a designed analogous system, we determine general modes of action for describing antiviral activities for both high-efficacy virus/AgCNP formulation pairs.

## RESULTS AND DISCUSSION

**Materials Synthesis and Colloidal Character.** Silver-modified cerium oxide formulations (AgCNPs) were synthesized in two distinct formulations (AgCNP1, AgCNP2), each utilizing different chemical reactions specific to aqueous silver. Several considerations were taken into account in designing the reported formulations with respect to silver incorporation with ceria and in biomedical performance; detailed in [Supporting Information \(SI\) Figure S1](#). AgCNP1 was synthesized via a previously developed, two-step procedure by our group ([Figure 1A](#)).<sup>25</sup>

Briefly, a solution containing AgCNP-like, silver-modified nanoceria, and silver secondary phases are formed via a forced-hydrolysis reaction. The product materials are washed with  $\text{dH}_2\text{O}$  and subsequently treated with ammonium hydroxide (as etchant as well as phase transfer complex: mediating aqueous dispersion of dissolved silver,  $[\text{Ag}(\text{NH}_3)_2\text{OH}]_{\text{aq}}$ ), followed by another washing step. AgCNP2 utilizes the stability of silver ions toward oxidation by  $\text{H}_2\text{O}_2$  ([Figure 1B](#)). Specifically, cerium and silver nitrate dissolution followed by  $\text{H}_2\text{O}_2$  addition leads to selective oxidation of  $\text{Ce}^{3+}$  over silver and the evolution of metallic silver phases on the ceria surface. The distinct synthesis conditions of these particles suggest a potentially disparate particle character AgCNP1. Where appropriate, results for AgCNP (AgCNP1 and AgCNP2) formulations were compared

against pure, related nanoceria formulations (CNP1 and CNP2, respectively).

Dynamic light scattering measurements are collected in Table 1 and relate a greater particle size for AgCNP1 particles ( $42.2 \pm$

**Table 1. Physicochemical Properties of AgCNP Formulations**

	AgCNP1	AgCNP2
Ce <sup>3+</sup> :Ce <sup>4+</sup> (%Ce <sup>3+</sup> ) (%)	25.8	53.7
[Ag]/[Ag+Ce] by XPS (%)	16.9	14.6
SOD Activity (% Inhibition)	97.9	99.2
Hydrodynamic Diameter (nm)	$42.2 \pm 4.6$	$31.6 \pm 2.4$
Zeta Potential (mV)	$22.4 \pm 0.9$	$24.1 \pm 1.3$
ICPMS Ce concentration (ppb)	$342.5 \pm 2.3$	$299.2 \pm 1.3$
ICPMS Ag concentration (ppb)	$24.1 \pm 1.03$	$74.9 \pm 1.21$
$E_{\text{corr}}$ (mV)	465.386	217.374
$I_{\text{corr}}$ ( $\mu\text{A}$ )	0.027	0.013
Beta <sub>a</sub> (mV)	681.7	617.0
Beta <sub>c</sub> (mV)	269.2	21.8

4.6 nm) compared to AgCNP2 ( $31.6 \pm 2.4$  nm). Further, zeta potential measurements indicate a greater surface potential for AgCNP2 over AgCNP1 ( $24.1 \pm 1.3$  and  $22.4 \pm 0.9$  mV, respectively). Particles from each synthesis were observed to demonstrate distinct fundamental and functional material character.

**Formulation Particle Crystallinity and Faceting.** As shown in Figure 2A X-ray diffraction (XRD) pattern of AgCNP1 sample, six major peaks indexed as (111), (002), (022), (113), (133), and (024) are related to cubic CeO<sub>2</sub> (ICSD 55284), along with low intensity peaks for metallic silver (ICSD 44387). The intensity of the (111) peak is relatively strong, as expected from related syntheses.<sup>25,26</sup> Peak broadening is clearly visible and apparent from the full-width half-maximum value  $3.318 \theta$  for (111) (fitted by Pseudo-Voigt function), in line with previous observation.<sup>25</sup> Scaling of major diffraction peak widths compared to unmodified samples, observed in our earlier study, were also observed in the current study. Additionally, (022) intensity is significantly greater than that of the (111) for AgCNP2 (Figure 2B), in contrast with typical observations and with AgCNP1. According to Zhang *et al.*, the (200) plane, despite having higher surface energy, can be formed when oxygen vacancy density reaches 50% within the facet, fulfilling a zero-dipole moment condition.<sup>27</sup> Additionally, the surface-dipole and related under-coordination can be mitigated by adsorption of solution components.<sup>28</sup> In the case of our synthesis, surface hydration will be pronounced, with hydroxylation being especially favored for [200]. Differences in surface faceting between each formulation suggest potential differences in catalytic activities and chemical reactivities.

**Surface Chemistry Analysis.** Figure 2C shows the XPS survey spectra of both AgCNP formulations. High resolution spectra of Ce 3d, Ag 3d (Figure 2D, and O 1s spectra (SI Figure S2) are acquired to highlight variations in particle chemical character.

The Ce 3d envelope ( $3d_{3/2}$  and  $3d_{5/2}$ ) (Figure 2D) revealed characteristic mixed valency (Ce<sup>3+</sup>/Ce<sup>4+</sup>) with peaks identified as  $v_o$ ,  $v'$ ,  $u_o$  and  $u'$  related to Ce<sup>3+</sup> and peaks described as  $v$ ,  $v''$ ,  $v'''$ ,  $u$ ,  $u''$ , and  $u'''$  to Ce<sup>4+</sup> oxidation states.<sup>29</sup> The relative concentration of Ce<sup>3+</sup> in each formulation has been estimated using the integrated peak area ratio [IPAR<sub>i</sub> = ACe<sup>3+</sup>/total area,

where 'A' represents the summation of Ce<sup>3+</sup>-related peak areas].<sup>30</sup>

Per this equation, AgCNP1 samples possess 22% and AgCNP2 60.9% of cerium as Ce<sup>3+</sup>. Ag 3d spectra (Figure 2D) collected for both formulations exhibited a doublet ( $3d_{3/2}$  and  $3d_{5/2}$ ) centered at 368.2 and 374.2 eV, related to metallic Ag (Ag<sup>0</sup>).<sup>31–33</sup> In addition, a doublet at 367.5 and 373.2 eV ascribed to Ag<sup>+</sup> is observable only for AgCNP1 (with 73.8% of silver in Ag<sup>0</sup> state).<sup>31–33</sup> The observed proportion of Ag<sup>0</sup> states suggest that silver is predominantly metallic, in agreement with the previous report.<sup>31–33</sup> In the case of AgCNP2, the Ag 3d spectra are comprised of only Ag<sup>0</sup> metallic state peaks centered at 368.2 eV (Ag  $3d_{5/2}$ ) and 374.3 eV (Ag  $3d_{3/2}$ ).<sup>31–33</sup> It is worth emphasizing that the full-width half-maximum value for metallic Ag<sup>0</sup> in the Ag 3d peak is increased in both formulations ( $\sim 1.25$  eV) compared to pure silver ( $\sim 150$  nm diameter particles) nanopowder ( $\sim 0.76$  eV) (SI Figure S3). This change can be ascribed to decreasing silver-phase dimensions and related confinement effects, as well as decreased final state electronic screening.<sup>34</sup>

**Particle Morphology and Dry Size.** The structural characteristics of AgCNPs were studied using high-resolution transmission electron microscopy (HRTEM). As shown in Figure 2E AgCNP1 particles are uniform, spherical, and 15–20 nm in size. Figure 2E (inset) clearly shows that the Ag-particles (black dots) were decorated as  $\sim 2$  nm crystallites on individual CeO<sub>2</sub> nanoparticle surfaces ( $\sim 20$  nm in diameter with 3–5 nm primary crystallites) (ceria phase:  $21.2 \pm 4.1$  nm; silver phase:  $2.7 \pm 1.6$  nm). The HR-TEM image from Figure 2F shows crystallites with estimated interplanar spacing 0.233 and 0.326 nm (determined via Inverse Fast Fourier Transform (IFFT) analysis) corresponding to the (111) planes of Ag and CeO<sub>2</sub>, respectively. The selected area electron diffraction patterns of AgCNP1 (Figure 2G) show *halo*-like patterns, indicating nanocrystalline nature. Inconsistent with the greater silver amount observed for AgCNP2 relative to AgCNP1 by ICPMS (Table 1), the morphological features of AgCNP2 particles from HRTEM (Figure 2H) show particles defined by clear ceria and silver phases (ceria phase:  $4.84 \pm 0.78$  nm; silver phase:  $14.66 \pm 2.84$  nm). It should be noted that ICP-MS values determined silver content is distinct from the value determined in XPS (Figure 2D). Specifically, mass spectrometry provides the total silver content in a sample, whereas XPS details the content near the material surface ( $< 5$  nm) as a consequence of the technique/method. Therefore, elemental analysis of a material will be skewed in representing composition: effectively over-representing components at the material surface (i.e., silver surface phases). An additional HRTEM image focusing on a single CeO<sub>2</sub> ( $\sim 5$  nm in size) (interplanar spacing: 0.326 nm of (111) for cubic ceria) with Ag ( $\sim 5$  nm in size) (interplanar spacing: 0.234 nm, for (111)) nanoparticle (Figure 2I,J) revealed a well-resolved interface between the two material phases. Additional TEM images are provided in SI Figure S4 for both formulations. Given the wealth of material characterization data for our AgCNPs and related control samples, many conclusions may be drawn specific to each formulation.

**Silver-Modified Nanoceria Proposed Formation Mechanism.** In another study, it was observed that incorporation of silver onto ceria substrate led to cerium site reduction and, in most tested instances, an oxidation of silver atoms localized at the ceria–silver interface for larger clusters.<sup>35,36</sup> The ability of ceria to hold silver in a positive oxidation state was observed experimentally in the same study as

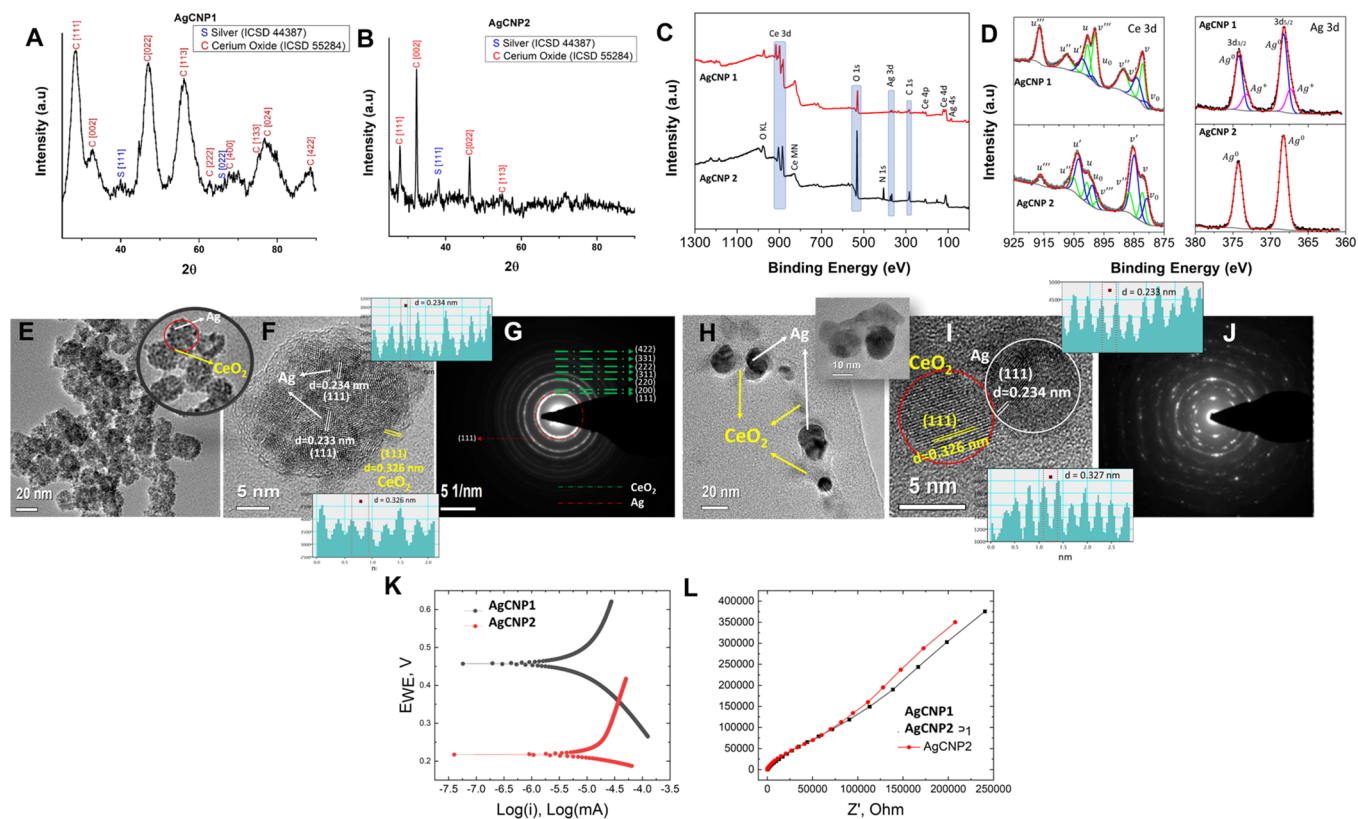


**Figure 2.** Materials characterization. (A and B) shows XRD patterns of silver-modified/-decorated CeO<sub>2</sub> nanoparticles (AgCNP1 and 2) showing major peaks belonging to CeO<sub>2</sub> (ICSD 55284) and minor peaks belonging to silver metal (ICSD 44387) signifying abundance of cerium oxide phase with traces of silver metal; (C) XPS survey of AgCNP1 and 2, (D) Deconvoluted Ce (3d) spectrum of AgCNP1 and 2 can be distinguished according to their oxidation states (Ce<sup>3+</sup>, shown in blue color; Ce<sup>4+</sup>, shown in green color) and Ag (3d) envelope shows both metallic (Ag<sup>0</sup>) and oxidized (Ag<sup>+</sup>) silver in AgCNP1, whereas only metallic silver-related signals are observed in AgCNP2. (E) HRTEM image of AgCNP1 showing spherical particles (size ~20 nm) enriched with Ag nanoparticles (ceria phase: 21.2 ± 4.1 nm; silver phase: 2.7 ± 1.6 nm). (F) HRTEM image of AgCNP1 showing crystallites with lattice fringe *d*-spacings of approximately 0.326 and 0.233 nm (determined by Inverse Fast Fourier Transform (IFFT)) relating to the individual (111) planes of Ag and CeO<sub>2</sub>, respectively. (G) SAED patterns related to AgCNP1 confirm particle crystallinity, with crystal planes determined and noted in the image, (H) Low magnification HRTEM micrograph showing general size and morphological character of AgCNP2 particles. (I) Higher magnification, HRTEM images of AgCNP2 particles highlight the observed two-phase character of individual particles: with 5 nm ceria particles in single interface with comparably-sized silver particles (ceria phase: 4.84 ± 0.78 nm; silver phase: 14.66 ± 2.84 nm). (J) Distinct lattice fringes in SAED patterns confirm crystallinity of AgCNP2 particles. (K) Tafel analysis for AgCNP1 and 2 showing distinct corrosion potentials for each formulation (465.386 and 217.374 mV, respectively). Measured *E*<sub>corr</sub> values are substantially more noble than pure silver (−150 mV, determined experimentally) suggesting a stabilization of silver phases by cerium oxide with AgCNP1–250 mV more noble than AgCNP2. Further, the in situ formation of each component may improve the registry (or generally lower interfacial energy) and thereby charge transfer at/across the interface, producing a more cathodic *E*<sub>corr</sub> value. (L) Nyquist representation of AgCNP1 and 2 from 10 Hz to 100 kHz; particles demonstrate near identical character at high frequency: ascribed to the common buffer/electrolyte character used in each testing and the insulating characters of the particle films.

well as in similar investigations.<sup>35,37</sup> Authors in another experimental study note the formation of a silver oxide layer separating metallic silver from ceria phases, which undergoes reduction over time under calcination.<sup>38</sup> Additionally, it was found in experimental and computational investigations that Ag<sup>+</sup>-species could substitute for cerium atoms at/near the surface of ceria substrates: lowering oxygen vacancy formation energy.<sup>36</sup> In our study, little difference was observed for Ce<sup>3+</sup> surface fraction relative to pure phase ceria particles synthesized by similar methods (data not shown), though the fractions were significantly different between AgCNP formulations (AgCNP1:25.8, AgCNP2:53.7%). The absence of greater Ce<sup>3+</sup>-fraction suggests that the formation of silver surface phases do not impart a significant reduction of cerium. However, it was observed in a computational study that interaction of silver with ceria is significantly more favorable at vacancy sites.<sup>35,36</sup> These interactions occur with silver coordinating to Ce<sup>3+</sup>-sites forming

a physical complex.<sup>36,37</sup> Interestingly, experimental studies have also shown an increase in surface vacancy density leads to an increased silver nanoparticle number density at the material surface, at fixed silver concentration. It has been stated in several studies that Ag<sup>+</sup> are effectively pinned to oxygen vacancies, in support of the observed modulation in silver nanoparticle density.<sup>35</sup> Similarly, we observe a high number density of silver nanoparticles at AgCNP1 particle surface, which shows a Ce<sup>3+</sup> fraction within the range measured in the referred study (0 to ~30%). Additionally, XPS measurements (Figure 2D) show a Ag<sup>+</sup> signal contribution which may be ascribed to silver atoms substituted into the ceria phase surface. It has been noted in many studies that such substitutions can lead to high catalytic activity, due in part to decreasing oxygen vacancy formation energy noted above.<sup>35,39</sup> Alternatively, Ag<sup>+</sup> may arise from formation of a thin silver oxide interlayer separating silver and ceria phases, similar to that observed by Aneghi *et al.* The

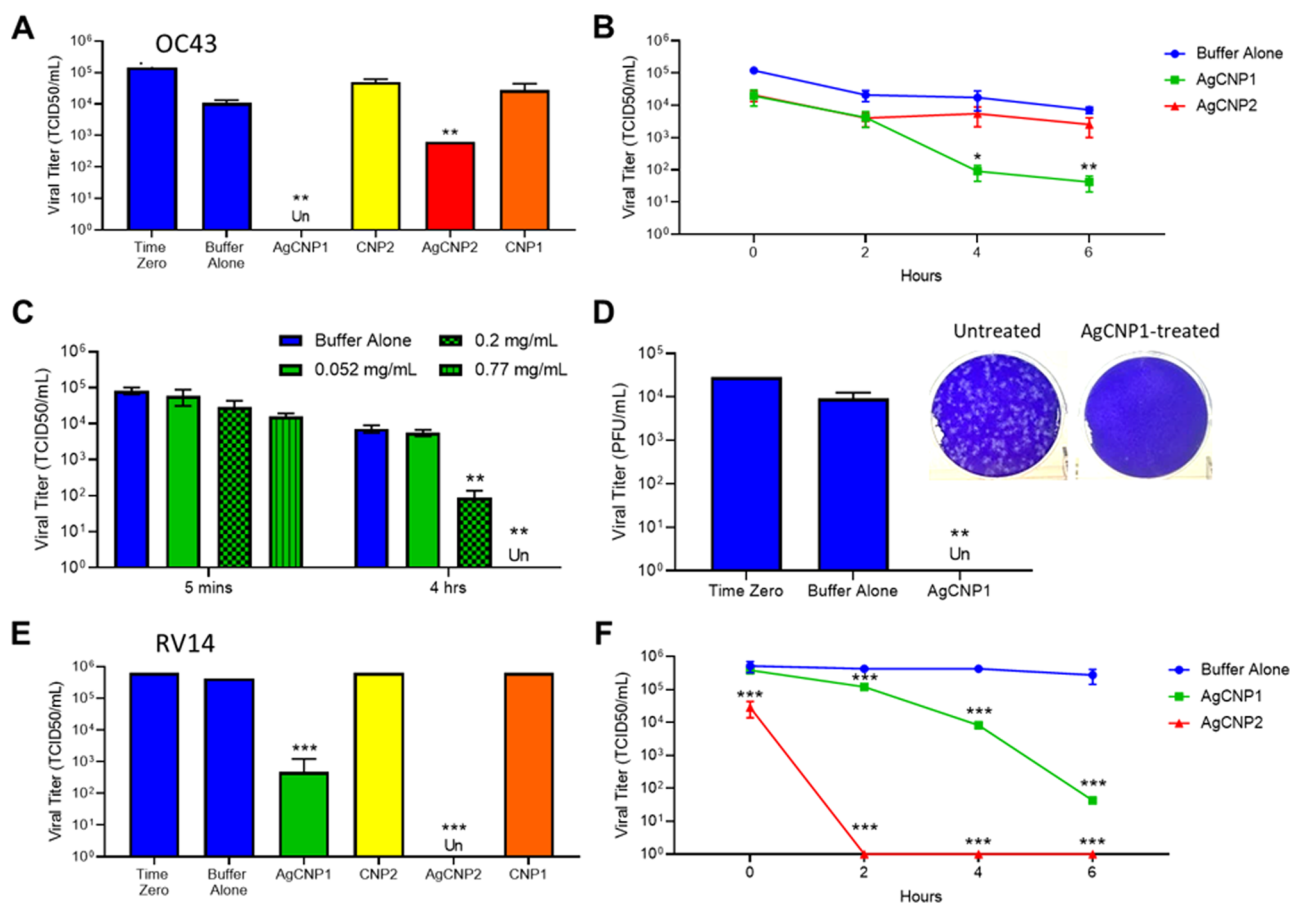


**Figure 3. Effect of AgCNP on Virus Infectivity.** (A, B) Samples of OC43 were incubated at room temperature for 6 h (A) or for the indicated times (B) with buffer alone (blue bars and lines), or with 0.2 mg/mL AgCNP1 (green), CNP2 (yellow), AgCNP2 (red), or CNP1 (orange). Remaining infectivity was determined by TCID<sub>50</sub> assay. A sample taken prior to addition of nanoparticles is indicated as time 0. Values are the mean of three independent samples, with error bars representing the standard deviation. Infectivity of OC43 virus showed high sensitivity to AgCNP1, with lower sensitivity to AgCNP2. (C) 10<sup>5</sup> TCID<sub>50</sub> units of OC43 were incubated at room temperature with buffer alone (blue bars) or the indicated concentrations of AgCNP1. Remaining infectivity was determined after 5 min or 4 h by TCID<sub>50</sub> assay. Values are the mean of three independent samples, with error bars represent the standard deviation and show dose-dependent inactivation of OC43 infectivity. (D) 10<sup>4</sup> PFU of OC43 was incubated with buffer alone or with 0.77 mg/mL AgCNP1 for 4 h at room temperature before determining remaining number of plaques. Representative plaques and an intact monolayer are shown in the top panel. (E, F) Samples of RV14 were incubated at room temperature for 6 h (E) or for the indicated times (F) with buffer alone (blue bars and lines), or with 0.2 mg/mL AgCNP1 (green), CNP2 (yellow), AgCNP2 (red), or CNP1 (orange). Remaining infectivity was determined by TCID<sub>50</sub> assay. A sample taken prior to addition of nanoparticles is indicated as time 0. Values are the mean of three independent samples, with error bars represent the standard deviation. (F) Time-dependent inactivation of RV14 infectivity by AgCNP2, which is different from the sensitivity of OC43.

absence of Ag<sup>+</sup> peak in AgCNP2 spectra may occur due to the significant peak broadening seen in XPS spectrum (Figure 2D), preventing the resolution of the peak. Further, the greater number density of silver phases observed on AgCNP1 surfaces would lead to a greater total interface area, as compared with the relatively small interfacial area produced by the larger more distinct silver phases of AgCNP2 (leading to a substantially lower Ag<sup>+</sup> signal). Interestingly, AgCNP2 particles show large silver nanophases in interface with comparably sized ceria phases (Figure 2H) and even greater fraction of Ce<sup>3+</sup> relative to AgCNP1. While this degree of reduction was not produced in other studies, some have utilized higher fractions of silver.<sup>35</sup> In these studies, highly reduced ceria surfaces preferentially nucleated silver with silver phases spreading across the surface. For AgCNP2, it is reasonable that the high fraction of Ce<sup>3+</sup>-sites allowed facile coalescence or surface diffusion of silver adatoms leading to the evolution of observed silver phases. Alternatively, stabilization of Ag<sup>+</sup> by solution peroxide may also limit adsorption at the ceria surface: leading to slow growth of

ceria-coordinated silver phases from solution. Peroxide stabilization of Ag<sup>+</sup> may also explain the lack of Ag<sup>+</sup> peaks in the XPS spectrum: preventing its availability for substitution into ceria during particle formation.

#### Bandgap and Conduction Band Level Measurements.

Conduction band position and bandgap were determined via Tauc analysis (Table 1) and ultraviolet photoelectron spectroscopy (UPS) (additional discussion for Tauc plot SI Figure S5, UPS valence band analysis SI Figure S6). In each case, materials from both formulations were observed to have narrower bandgaps, determined through Tauc analysis/plotting, as compared to pure control syntheses (2.81 v. 2.88 for AgCNP1 and 3.53 v. 4.12 eV for AgCNP2). AgCNP2 bandgap (−0.7 eV) narrowing relative to the pure nanoceria sample is not well understood, though is likely influenced by absorption signal from the silver phase. UPS spectrum collected for AgCNP1, interestingly, shows a significant intensity at the valence band region (SI Figure S6). This level population is ascribed to the presence of silver; potentially at the interfaces between ceria and

silver phases, given the greater total energy (due, especially, to strain and redox) of these phase components. Decreasing bandgaps for each material, versus controls, and silver introduction suggest potentially greater surface reactivity beyond that of control ceria. Therefore, the activity of both AgCNP formulations were assessed for ROS-scavenging/generating activities.

**Enzyme-Mimetic Character from Chemical Assay.** ROS generating/scavenging activity in ceria can be approximated as their relative catalase- and SOD-mimetic activities. Assays for each activity were conducted as a measure of the effects of silver modification on these reactions/reactivities (and thereby, potential viral disinfection activity). SOD-mimetic activity was recorded for both AgCNP samples with each demonstrating high scavenging activity (Table 1) (97.9 and 99.2% activity for AgCNP1 and AgCNP2, respectively). Interestingly, silver nitrate control similarly showed very high scavenging activity suggesting silver incorporation may lead to the particles' total ability to scavenge radicals, along with the general observation that nanoceria formulations having higher amounts of reduced states (25.8 and 53.7% for AgCNP1 and 2, respectively) at their surface tend to possess this activity. However, it should be noted that theoretical and computational studies into silver-modified ceria surfaces demonstrate localization of  $\text{Ce}^{3+}$  reduced states to the ceria–silver interphase.<sup>36</sup> It should therefore be noted that AgCNP1 particles are observed to be highly poly crystalline with silver crystallite phases studding the particle surface (Figure 2E). It is likely a large fraction of  $\text{Ce}^{3+}$  are localized to the silver–ceria interfacial regions (Figure 2F). Interestingly, despite observed high SOD activity, AgCNP1 also demonstrates a marked catalase activity (79.6%); with AgCNP2 showing negligible activity. This contrasts with unmodified nanoceria, which show inverse relationships between material catalase and SOD activities. Further, silver nitrate control did not possess significant catalase activity (data not shown). Given the substantial activities in each assay for AgCNP1, it appears that each phase in the material contributes activity: giving the modified formulations greater functionality over each pure phase material. The lack of catalase activity in AgCNP2 likely arises from the high density of  $\text{Ce}^{3+}$  at the material surface in interface with solution (due to limited total ceria–silver interfacial area for particles). The observed enzyme-mimetic activities for each formulation suggest their potential for use in disinfection applications.

**Electrochemical Characterization.** Electrochemical measurements (Figure 2 K,L) were performed to determine the activity of silver phases in the AgCNP formulations along with their susceptibility to electron transfer processes. AgCNP1 evidenced a larger Tafel potential (Table 1) than AgCNP2 (465.4 vs 217.4 mV, respectively), suggesting a greater stability toward electron transfer and a more noble oxidation character. Interestingly, AgCNP1 demonstrated a Tafel current twice the value observed for AgCNP2 (0.027 and 0.013  $\mu\text{A}$ , respectively). These values are relatively low, suggesting high electrochemical impedance and overall stability for silver phases in each formulation. However, greater current value for AgCNP1 at higher potential may be understood from XPS spectra wherein a fraction of sample silver content was found in positive oxidation state. Penetration of  $\text{Ag}^+$  into the ceria surface/subsurface as a partly oxidized silver/ceria interlayer would increase the Tafel potential (i.e., have a stabilizing effect on the silver phase) while simultaneously improving registry of the phases at their interphase, improving charge transfer as Tafel current.<sup>36</sup>

Significantly greater anodic  $\beta$ -values over cathodic observed in Tafel analysis (Table 1) for both samples suggest electron transfer at Tafel potentials are kinetically favored by oxidation. Literature data corroborate the stabilization effects (positive overpotential) of the ceria phase for both formulations with AgCNP1 posing a significantly greater effect (relative overpotential:  $\sim 250$  mV).<sup>35,36</sup> Further, measurements with silver nitrate suggest silver from AgCNP particles do not undergo significant, spontaneous dissolution (absence of related redox peak). Release of silver ions is noted in other studies to effect a general toxicity toward biological systems.

**Selective Inactivation of Two Human Respiratory Viruses with AgCNP1 and AgCNP2.** To determine the extent to which nanoceria and AgCNPs can inactivate human coronavirus OC43, reactions were prepared to include  $10^5$  infectious units (TCID50) of virus/mL (Figure 3A).  $10^5$  TCID50/mL input virus was determined as time zero infectivity. OC43 incubation with buffer alone resulted in  $\sim 1$  log loss of infectivity (Figure 3A), consistent with prior work on the stability of coronaviruses in aqueous solutions. The slight instability of enveloped RNA viruses contrasts with the finding that the infectivity of nonenveloped Rhinovirus was stable in aqueous solutions.<sup>40</sup> After a 6 h incubation, the buffer alone control reactions had  $10^4$  TCID50/mL remaining infectious virus. The unmodified nanoceria formulations had little effect on virus titer with reactions remaining at  $\sim 5 \times 10^4$  TCID50/mL. Strikingly, AgCNP1 treatment resulted in complete inactivation, whereas AgCNP2 reduced infectious virus titer to  $\sim 10^3$  TCID50/mL. A time-course study was conducted with reactions prepared as described above. Infectious virus was determined after incubation for zero, 2, 4, and 6 h (Figure 3B). As early as 4 h, AgCNP1 treatment reduced OC43 virus titer from  $10^5$  TCID50/mL to  $<10^2$  TCID50/mL. Taken together, these data suggest AgCNP1 was highly effective at inactivating coronavirus OC43 and that AgCNP2 had a modest capacity for inactivation. Additionally, studies into the continued disinfectant activity of both formulations were collected as virus rechallenge studies (SI Figure S7). In considering the relative efficacy of each particle formulation toward a given virus species as inactivation by log-value reduction, U.S. EPA (Environmental Protection Agency) standards of  $> \log(3)$  reduction were used as a benchmark of significant activity. Results from these studies suggest a catalytic/regenerative activity for the particles: showing virus inactivation at similar rates to those observed in the initial incubation.

We next determined the extent to which nanoceria and AgCNPs can inactivate the human respiratory pathogen rhinovirus 14 (RV14), a nonenveloped icosahedral RNA virus. (Figure 3E)  $6 \times 10^5$  TCID50/mL input RV14 virus was determined and represented as time zero. After 6 h incubation, buffer-alone reactions retained the input infectivity of  $6 \times 10^5$  TCID50/mL. Unmodified nanoceria formulations had little effect on RV14 infectivity. Importantly, AgCNP1 treatment reduced infectious virus titer to  $5 \times 10^2$  TCID50/mL, whereas AgCNP2 treatment resulted in complete inactivation of infectious virus. In a time-course study, incubation of  $6 \times 10^5$  TCID50/mL of RV14 with buffer alone showed no loss of infectivity over a 6 h incubation (Figure 3F). In contrast, there was a very rapid loss of RV14 infectivity to undetectable levels by 2 h incubation with AgCNP2. Incubation with AgCNP1 showed slower inactivation of RV14 compared to AgCNP2, with virus titer being reduced to  $\sim 10^2$  TCID50/mL after 6 h. Taken together, these data demonstrate AgCNP formulations can

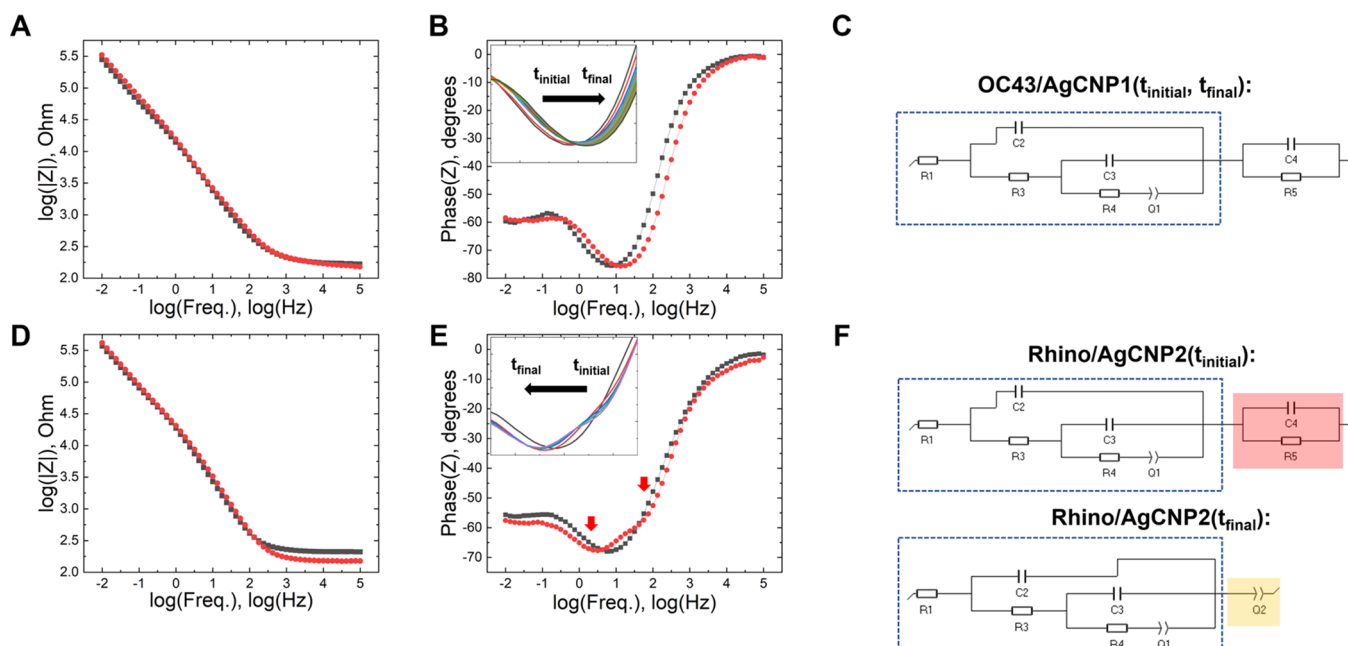


**Figure 4.** *In situ* measurements of AgCNP-Virus interactions via impedance spectroscopy. First row (A–C) incubation of AgCNP1 with OC43, enveloped coronavirus; second row (D–F) related to AgCNP2 incubation with nonenveloped rhinovirus measured at regular time intervals of 30 min (total 2 and 4 h for Rhinovirus and OC43 virus incubations, respectively). Impedance data (A,B; D,E) plotted in the Bode representation with (A,D) relating impedance magnitude to frequency and (B,E) relating phase to frequency for each formulation/virus pairing. AgCNP1/OC43 interaction shows a common impedance v. frequency character (A) for initial and final time points and (B) shows a characteristic, apparent shift in phase to higher frequencies ( $+\Delta\log(0.4)$  Hz) with increased incubation time. AgCNP2/Rhino impedance v. frequency (B) shows a decreasing trend in impedance for frequencies above 100 Hz with increasing incubation time. Phase v. frequency shows distinct character for the final time point relative to initial time point and to the character observed for AgCNP1/OC43 (B). The initial curve form has a feature centered at  $\sim\log(0.9)$  Hz which appears to broaden leading to features at  $\log(0.5)$  and  $\log(2.0)$  Hz. Circuit fittings for each particle-virus pair (C and F for AgCNP1/OC43 and AgCNP2/Rhinovirus, respectively) reflect the specific interactions between particle formulation and certain tested viruses. Circuit models for all spectra show elements and connectivity/topology common for all measurements (highlighted in dotted box) reflecting solution resistance (buffer character), electrode charge transfer resistance, and resistance/capacitance character of a biological dropcast film. The circuit diagram portions common for all measurements are represented in several bioimpedance models (e.g., Giaevers-Keese and Hayden cell layer models). The specific character/action of tested AgCNP-virus pairings are apparent in the highlighted circuit regions. Specifically, variation in phase/frequency over time for AgCNP1/OC43 (B) denotes capacitive behavior suggesting particle interaction with the virus surface (modulation of capacitive/electrical double-layer). In contrast, AgCNP2/Rhinovirus phase/frequency measurements (E) show a change in circuit diagram composition over time: suggesting evolution of an emerging system feature with a specific time constant and a frequency-dependent character. The observed behavior can be represented by a constant phase element ( $f, t_{\text{final}}$ ) reflecting a concurrent, frequency-dependent change in real and imaginary impedance. The observed behavior can be related to chemical changes in the Rhinovirus film layer occurring at the virus surface: modulating capacitive (i.e., double-layer) character while effecting an increased resistance character (e.g., protein oxidation).

inactivate RV14 infectivity, with AgCNP2 having a more potent anti-RV14 effect. In comparing the specific antiviral activities for these virus/particle systems, we see up to 2 orders of magnitude decrease in active material concentration, at comparable concentrations, for AgCNPs relative to common organic disinfectant agents.

**In Situ Bioelectrochemical Impedance Spectroscopy of AgCNP Disinfectant Activity.** The substantial disinfectant activities demonstrated by both formulations to specific virus species, suggest distinct modes of action. In order to probe the character of each, EIS was performed for AgCNP1/OC43 and AgCNP2/Rhinovirus (Figure 4). Herein, the impedance is measured with the data fit to simple circuit diagrams with circuit elements representing physicochemical components/processes. In recent years, the technique has been applied to the study of changing cell character upon physical or chemical stimulation.<sup>41,42</sup> Among these studies, conditions wherein the cell membrane character changes are the most often investigated. A simple interpretation of cell-substrate EIS data is given by the ECIS model of Giaevers and Keese wherein impedance

components are deconvoluted as resistance to charge flow between biological components, as well as from regions between these components and the electrode substrate, and cell membrane capacitance.<sup>43,44</sup> In studies of cell health, these model components are diagnostic: with each changing upon introduction of toxic agents (e.g., as membrane pore-formation, retraction of focal regions, membrane oxidation).<sup>44</sup> Further, these responses are necessarily frequency-dependent with specific frequency bands identified for specific biological processes. In identifying changes to impedance spectra over time in the presence of test agents (e.g., AgCNPs), specific biochemical processes may be identified.<sup>44</sup>

In the presented study, test case impedance spectra were distinct from each other over the incubation periods (2 h for RV14 and 4 h for OC43) from the virus studies above (Figure 4): in support of the observed particle/virus dependence in virus inactivation studies (Figure 3). For AgCNP1 (Figure 4 A,B), spectra were collected over the 4 h disinfection period (SI Figures S8 and S9 for fitted equivalent circuit diagram values/diagrams at initial and final time points, respectively). The

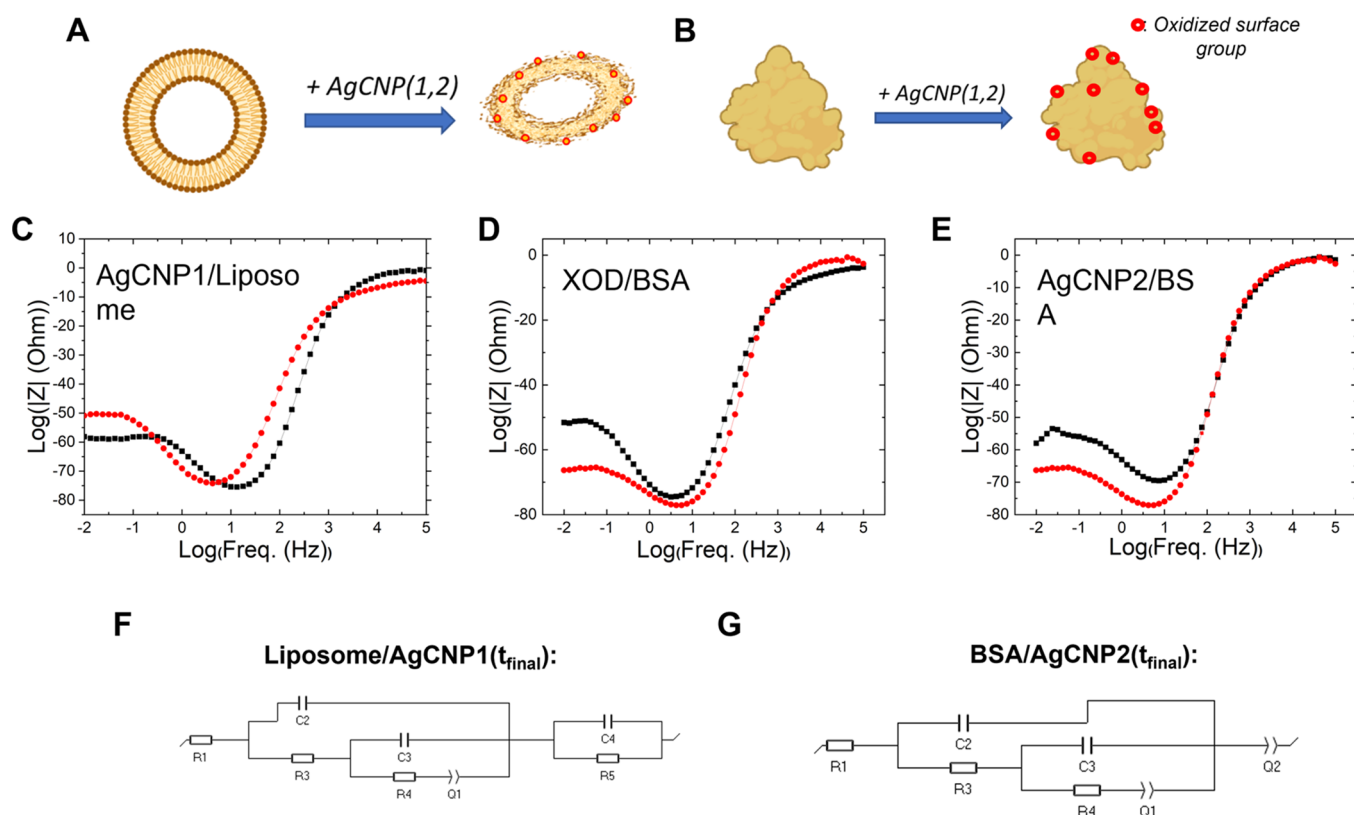


**Figure 5.** Electrochemical model of *in situ* AgCNP-virus interactions. Incubation of AgCNP1 and AgCNP2 with OC43 enveloped coronavirus and nonenveloped Rhinovirus, respectively, show distinct physicochemical interactions as differences in electrochemical impedance spectra over respective incubation times (AgCNP1/OC43:2 h, AgCNP2/Rhinovirus: 4 h). The noted differences are represented as cartoons for each of AgCNP1/OC43 (A; spectra character dominated by physical interaction between particles and virus membrane producing greater capacitive character) and AgCNP2/Rhinovirus (B; phase shift in capacitive element to lower frequencies and evolution of resistive character due to protein oxidation, surface alteration). Simplified, model electrochemical systems were designed and tested as analogs of AgCNP:virus systems to isolate/confirm proposed antiviral mechanisms ( $\sim 100$  nm liposomes representing coronavirus membranes and bovine serum albumin (BSA) globular proteins representing the solution-interfacing capsid proteins of nonenveloped Rhinovirus). Incubation of liposome-modified electrodes with AgCNP1 reproduces the phase/frequency shift (C) observed in the original particle-virus system (Figure 4B) and reflected in the fitted circuit diagram (F). The oxidative mechanism for AgCNP2/Rhinovirus was first approximated electrochemically through *in situ* oxidation of BSA films by a xanthine oxidase-acetylacetate reactive oxygen species-producing system (D) and compared against BSA films in the presence of AgCNP2 (E). Impedance spectra for each are comparable to that seen in Figure 4E for AgCNP2/Rhinovirus: suggesting a dominant chemical/surface oxidation mechanism for the particle/virus system. Spectral changes for each test system are represented through circuit diagram fitting as (G) with the diagram reflective of that seen for AgCNP2/Rhinovirus (Figure 4F).

spectra show a near-consistent impedance character with differences in magnitude only being evident at high frequencies (decreasing with time; 100 Hz to 100 kHz). There is a clear, time-dependent shift in phase “peak” (i.e., spectrum feature; apparent peak) to a lower frequency (frequency shift:  $-\Delta 0.4$  decades/Hz from  $\sim 1.2$  decades/Hz). These results are limited to the  $\alpha$ -dispersion region; we expect spectra changes to be associated with ionic diffusion, especially in the cell membrane, and physical interactions with the cell membrane.<sup>45</sup> AgCNP2 (Figure 4D,E) shows a similar initial spectrum character (SI Figures S10 and S11 for the fitted equivalent circuit values/diagram at initial and final time points, respectively). However, with increasing incubation time, the spectrum becomes more complex: appearing as two observable ‘peaks,’ ascribed to a time-dependent process not observable at early incubation times. In fact, the peak at 0.5 decades/Hz appears as a shift to lower frequencies of the “peak” in the initial spectrum, while the peak centered at 2.0 decades/Hz is completely distinct. Differences between these spectra corroborate the disparate particle–virus interactions and suggest the presence of an additional element in the related equivalent circuit diagram. Given the observed

change in phase/frequency values, data suggests a constant phase element component (impedance being dominated by resistance at increasing frequencies). Spectra fittings demonstrate these characters with a common diagram construction for all test cases, save for the variable elements (shown as colored regions in Figure 4 C,F), particular to specific AgCNP and virus interactions at defined time points. The variable elements being fit as a parallel resistor and capacitor for AgCNP1/OC43 and as a constant phase element for AgCNP2/RV14, as suggested by the phase vs impedance character. In particular, the parallel elements fit to the time-dependent behavior of the AgCNP1/OC43 interaction change in value from high resistance (387.8  $\Omega$ ) and moderate capacitance (24.7  $\mu\text{F}$ ) to significantly lower values of each (23.8  $\Omega$  and 6.3  $\mu\text{F}$ ). In particular, the resistance value changes precipitously with incubation. The results together corroborate the proposed particle/virus interaction leading to changes in membrane integrity/permeability; decreasing resistance related to the permeability and capacitance to the lowered membrane density and physical interaction with the oxide nanoparticle. The constant phase element variable component of RV14:AgCNP2 is a frequency-dependent

element that models an imperfect dielectric. In the case of this system, increasing incubation term leads to an increasingly resistive (initial value:  $R_5 = 99.44 \Omega$ ,  $C_4 = 6.73 \mu\text{F}$ ; final value:  $Q_2 = 83.5 \mu\text{F}\cdot\text{s}/a$ ,  $a_2 = 0.60$ ) character for the model dielectric, from the initial character similar to that seen for OC43 (SI Figure S8). In order to better interpret and assign the observed *in situ* character to specific physicochemical process, a physical model was developed, and relevant control reactions studied.

**Developing a Physical Model of Bioelectrochemical Impedance Spectroscopy.** Analog systems were produced with respect to RV14 and OC43 virus systems to identify the specific antiviral mechanisms produced during *in situ* EIS measurements. Therefore, two distinct systems were produced to model the dense protein structure of the RV14 surface (bovine serum albumin, globular protein) and the enveloped surface of OC43 (liposomes, commonly used as virus-mimetic vectors/virus-like particles). All measurements were performed in identical electrolyte conditions as those for the *in situ* measurements to control for solution-based impedance contributions and with the virus analog materials immobilized on a glassy carbon electrode. Liposomes were synthesized to the approximate dimensions ( $\sim 120$  nm) of the OC43 coronavirus to appropriately model physical interaction with AgCNP. In each case, the behavior of the analog material seemed to reflect the behavior observed for the related virus, with the corresponding AgCNP formulation dependence. In Figure 5, it is notable that the fitted spectra lead to equivalent circuits similar to the *in situ* data. For the Liposome/AgCNP1 system (Figure 5 A,F), we observe the variable elements are a parallel resistor and capacitor with this character retained over the incubation period (SI Figure S12 shows fitted equivalent circuit values/diagram; SI Figure S13 shows control Liposome/AgCNP2 measurement). However, we see the values of these elements change over the incubation period resulting in a related phase shift (frequency shift:  $\Delta 0.6$  decades/Hz). Related fitted materials for the BSA/AgCNP2 system (Figure 5 E,G) occur and relate to the RV14/CNP2 *in situ* data (SI Figure S14 shows equivalent circuit values/diagram). However, we see that the spectra in the analog system are less defined (i.e., peak-like features are less resolved) than those seen in the virus system. The slight variation in character can be ascribed to the small-scale differences among the systems (e.g., BSA globular structure versus RV14 dense, multi-protein surface). However, spectra suggest that the specific virus/particle and virus/analog interactions are similar. Given the evolution of additional resistive characters in the models, we determined to identify any specific chemical changes occurring. Therefore, an oxygen radical-generating system, known to induce lipid peroxidation through the simultaneous, proportional production of superoxide and  $\text{H}_2\text{O}_2$ , was used as a positive control for the activity (control measurements of liposome/xanthine: xanthine oxidase and BSA/xanthine:xanthine oxidase are collected in SI Figures S15 and S16, respectively).

In these experiments, the effects of the positive control for radical oxygen evolution were assessed via related changes in the spectrum. It was observed (Figure 5B) that oxidation reproduced the “additional peak” (centered at  $\sim 1.9$  decades/Hz) observed in the RV14/AgCNP2 system for the BSA/AgCNP2 spectrum (Figure 5C). The observed character was also reproduced for the Lipo/AgCNP1 system (SI Figure S9), confirming that the spectra character change in the viral system does not originate from a chemical attack in AgCNP1 incubation.

The detailed methodology allowed time-dependent, *in situ* measurements of virus-nanomaterial interactions. Given the direct nature of this technique and its limited perturbation of the biological system, it is reasonable that the results obtained closely reflect the true nature of interaction. Further, the frequency-dependent signal character allows deconvolution of contributing process signals. However, future studies will focus on providing precise characterization of these suggested interactions via methods more traditional to virology studies, such as imaging and gel electrophoresis.

## CONCLUSIONS

In the presented study, two formulations of cerium oxide nanoparticles were produced with surfaces modified by silver nanophases. Materials characterization shows that the silver components in each formulation are distinct from each other and decorate the ceria surface as many small nanocrystals (AgCNP1) or as a two-phase construct of ceria and silver with single interface (AgCNP2). Each synthesis further possesses distinct mixed-valency characters, with AgCNP2 possessing a more significant fraction of  $\text{Ce}^{3+}$  states relative to  $\text{Ce}^{4+}$  over AgCNP1. The distinct valence characters and incorporation of chemically active silver phases lead to high catalytic activities for each formulation. AgCNP2 possesses high superoxide dismutase (SOD) activity, while AgCNP1 possesses both catalase and SOD-like enzyme-mimetic activities, ascribed to the catalase activity of ceria and the superoxide dismutase activity from silver phases. Further, electrochemical analysis demonstrates that silver incorporated in each formulation is substantially more stable to redox-mediated degradation than pure silver phases: promoting an increased lifetime in catalytic applications.

Human respiratory viruses are a major public health concern and impose a huge burden on the economy and the health care industry. Here we show that AgCNP particles have selectivity in their ability to inactivate members of two major human respiratory virus families: AgCNP1 is potent against seasonal coronavirus OC43 (enveloped RNA virus), while AgCNP2 is potent against rhinovirus 14 (nonenveloped RNA virus). The outer surfaces of these two viruses differ substantially: coronaviruses have a relatively low density of protruding glycosylated spike-proteins that are imbedded in a phospholipid bilayer, whereas picornaviruses such as RV14 have a strictly organized nonglycosylated protein-only shell with repeating icosahedral symmetry.<sup>46</sup> These viruses also have very different steps in entry into cells to initiate an infection. Thus, the factors that dictate AgCNP selectivity for inactivating an enveloped versus nonenveloped RNA virus will require further biochemical and structural studies in the future. Based on prior work with serum-neutralization of other enveloped RNA viruses, these mechanisms could include (1) disruption of lipid membrane integrity, (2) protein denaturation at the virion surface, or (3) encapsidation of virions within AgCNP adsorbates.<sup>47</sup> Based on *in situ* data (Figure 4) and the related model data (Figure 5), we propose that the dominant physical interaction of AgCNP1 with the OC43 envelope is disrupting the lipid bilayer (observable in electrochemical experiment as changes to resistive/capacitive values), whereas the chemical reactivity of AgCNP2 with the protein shell of RV14 inactivates the virion through denaturing the proteins involved in receptor binding (as observed experimentally as evolution of the equivalent circuit diagram in *in situ* measurements). We present an approach to producing potent and versatile antiviral particles that will have wide applications for the treatment of other human pathogenic

viruses, including SARS-CoV-2, Ebola virus, Nipah virus, and enteroviruses, as well as emerging pathogens with pandemic potential.

## MATERIALS AND METHODS

**AgCNP formulations syntheses.** Two silver-modified cerium oxide nanoparticle formulations were synthesized and referred as AgCNP1 and AgCNP2. AgCNP1 was synthesized using a base-mediated forced hydrolysis method. First, 1.74 g of cerium nitrate hexahydrate was dissolved in 40 mL of dH<sub>2</sub>O under light stirring and 170 mg of silver nitrate dissolved in 10 mL of dH<sub>2</sub>O. The solutions were mixed, the stir speed increased, and the solution was titrated with 10 mL of 0.4 M sodium hydroxide. From here, the solution was washed 3x with dH<sub>2</sub>O. Pellet was resuspended in dH<sub>2</sub>O and ultrasonicated. Particle concentration (mass/volume) was determined by dry weight (dried at 65 °C overnight). Stock particle suspension was then ultrasonicated, as above, and diluted in 3% aq. NH<sub>4</sub>OH. Above solution was then stirred for 24 h. Solution was washed, resuspended in dH<sub>2</sub>O, and ultrasonicated in similar manner to earlier steps.

AgCNP2 particles: 109 mg of cerium nitrate hexa-hydrate (99.999% purity) was dissolved in 47.75 mL dH<sub>2</sub>O in 50 mL square-cornered glass bottle. 250  $\mu$ L of 0.2 M aq. AgNO<sub>3</sub> (99% purity) was added to the cerium solution above with the solution vortexed. From here, 2 mL of 3% hydrogen peroxide was added quickly to the above solution followed by immediate vortexing. Solution was stored in dark condition at room temperature with the bottle cap loose to allow for release of evolved gases; solutions were left to age in these conditions for up to 3 weeks (monitoring solution color change from yellow to clear). Particles were then dialyzed (in cellulose dialysis tubing) in 2 L glass beaker over 2 days in 2 L of dH<sub>2</sub>O changed every 12 h and stored in the same conditions as for aging. Particles are ultrasonicated prior to any further use.

**Materials Characterization.** The morphology and dried size of the nanomaterials produced in this study were determined using a Philips Tecnai 300 kV HRTEM. All samples were first dried on holey carbon TEM grids to at room temperature and then stored under vacuum. Phase contributions to particle size were determined by measuring 25 particles from each formulation using the GATAN Micrograph software. UV-vis spectrophotometry was performed using a PerkinElmer spectrophotometer over a range of 220 to 800 nm. X-ray photoelectron spectroscopy was used to characterize the materials compositions as well as changes to their surface states. Additionally, UV photoelectron spectroscopy was performed to characterize the valence states of each sample as well to determine their bandgaps. X-ray diffraction analysis was done using Empyrean Panalytical and used XPert Highscore software for data analysis. CuK $\alpha$  (1.54 Å) radiation was used for diffraction. ESCALAB-250Xi spectrometer at room temperature in ultrahigh vacuum chamber (below  $7 \times 10^{-9}$  mbar) using a monochromatic Al-K $\alpha$  radiation source, operating at a power of 300 W (15 kV, 20 mA). The spot size of the beam was 650  $\mu$ m. C 1s peak at 284.6 eV was used as a reference for calibration. Avantage Peakfit software was used to deconvolute XPS spectra. For reference XPS-simplified spectra from Thermo Scientific Web site were compared against the obtained spectra as well as comparisons to literature values. Dynamic light scattering and zeta potential measurements were performed in 0.1 M tris-Cl buffers (pH 7.5) using a Zeta-sizer Nano from Malvern Instruments to determine the hydrodynamic diameters and zeta potentials, respectively, of each AgCNP formulation. The concentration of Cerium and Silver were measured using inductively coupled plasma-mass spectrometry (ICP-MS). Agilent 7700X ICP-MS instrument was used in Trace Evidence Analysis Facility at Florida International University to measure the level of Cerium concentration and Finnigan Element-2 (HR-ICPMS) was used to measure silver concentration at Cerium Laboratories, Austin, TX. *ICP-MS sample preparation:* 1 mL of the stock AgCNP formulations (1 mg/mL) was digested for 48 h in 2 mL 35% nitric acid by heating at 80 °C in the conventional oven. Post digestion, the suspensions were diluted to working suspension of a mass concentration of  $\sim$ 500  $\mu$ g/L or (parts per

billion (ppb)) with ultrapure water, keeping nitric acid concentration at 5% (necessary for ICPMS measurement).

**Electrochemical Measurements.** Electrochemical measurements were performed with a potentiostat from BioLogic. A round disk glassy carbon electrode was used as a working electrode with a saturated (KCl) calomel electrode as a reference electrode and platinum mesh counter electrode. Cyclic voltammetry was performed from 1.0 V to  $-0.3$  V for 50 cycles at 1 V/s in 1 M H<sub>2</sub>SO<sub>4</sub> following slurry polishing on a microfiber pad to clean the working and reference electrodes previous to experiments. Experimental cyclic voltammetry experiments were performed from 1.0 V to  $-0.3$  V for 50 five cycles at 1 V/s. For each experiment, changes to the voltammograms were monitored with successive cycles and found to be stable. Potentiometric electrochemical impedance spectroscopy (EIS) was performed from 10 mHz to 1 MHz with a root sinus frequency value of 0.2. For these experiments, 20  $\mu$ L of 1 mg/mL sample (from each of the AgCNP samples) was dropcast onto the glassy carbon electrode and dried under a gentle stream of nitrogen. Tafel analysis was performed by first monitoring sample open circuit potential until stable and performing linear sweep voltammetry from 0.1 V more anodic than open circuit potential. Voltammetry was performed at 20 mV/min in anodic ongoing potential to 1.0 V. The modified electrode was then dipped in three washes of dH<sub>2</sub>O to remove any weakly bound particles. *In situ* bioimpedance spectra were collected with parameters similar to those used in nanomaterial characterization though at open circuit potential (after equilibrating in tris buffer). Either OC43 or Rhinovirus was allowed to dry on a clean glassy carbon electrode surface and was dipped three times to remove salts and weakly adsorbing virus particles. Electrochemical impedance spectra were then collected with AgCNP1 or 2 dispersed in tris-HCl buffer at a concentration of 20  $\mu$ g/mL in 4 mL working volume over similar time periods as for infectivity assays.

**Enzyme-Mimetic Assay.** Superoxide dismutase mimetic activity was determined using a SOD assay kit (Dojindo, SKU: S311) according to the manufacture's instruction. Catalase mimetic activity was investigated by the protocol described by Pirmohmed *et al.*<sup>15</sup> The Amplex Red Hydrogen Peroxide/Peroxidase assay kit (Invitrogen, Cat# A22188) was used to measure H<sub>2</sub>O<sub>2</sub> levels. A microplate reader (FLUOstar Omega, BMG LABTECH) was used to detect the fluorescence of resorufin (excitation at 571 nm and emission at 585 nm). An H<sub>2</sub>O<sub>2</sub> standard curve was generated and used to calculate the H<sub>2</sub>O<sub>2</sub> concentration in each sample. 50  $\mu$ L of sample, at a fixed common concentration for all samples, is preincubated with 50  $\mu$ L of 8  $\mu$ M H<sub>2</sub>O<sub>2</sub> for 25 min in 96-well plates. Then 100  $\mu$ L of working solution (100  $\mu$ M Amplex Red reagent and 0.2u/mL HRP) was added and allowed to incubate at room temperature for 30 min before the fluorescence readings were taken. CAT activity is calculated by dividing the final H<sub>2</sub>O<sub>2</sub> concentration in each sample by the initial H<sub>2</sub>O<sub>2</sub> concentration and multiplying with 100%.

**Cells, Viruses, and Infectivity Assays.** Cultures of HCT-8 cells were grown in Roswell Park Memorial Institute medium (RPMI 1640, Gibco, Thermo Fisher Scientific) supplemented with 10% heat inactivated fetal calf serum (HI FBS, Gibco, Thermo Fisher Scientific). Cultures of RD and HeLa cells were grown in Dulbecco modified Eagle medium (DMEM, Gibco, Thermo Fisher Scientific) supplemented with 10% HI FBS.

Human Coronavirus OC43 (ATCC, catalog number VR-1558) was grown in HCT-8 cells at 33 °C. Media collected at 4 days post infection (pi) was centrifuged, cell debris was discarded, and then was adjusted to include a 1:20 dilution of Bovine Albumin Fraction V (BSA, 7.5% solution, Fisher). Aliquots were quickly frozen using liquid nitrogen and stored at  $-80$  °C. OC43 stocks were quantified using a standard 50% Tissue Culture Infectious Dose assay (TCID<sub>50</sub>) on confluent RD cells in 96-well plates (Falcon, Thermo Fisher Scientific). Briefly, solutions were serially diluted in DMEM containing 1:20 BSA. After incubation with diluted virus solutions for one hr at 33 °C, cells were washed and replaced with DMEM containing 2% HI FBS. After a 4 day incubation at 33 °C, cells were washed with PBS+ and stained with a 1% crystal violet solution containing 20% ethanol, 3.7% formaldehyde and PBS for 30 min. TCID<sub>50</sub> values were calculated by the Spearman & Kärber

algorithm as previously described.<sup>48</sup> OC43 plaque assay was carried out on RD cells as described by Bracci *et al.*<sup>49</sup>

Human Rhinovirus 14 (RV14, ATCC, catalog number VR-284) was grown in HeLa cells at 33 °C. Cell monolayers and dislodged cells were harvested and processed by three rounds of quick freezing in liquid nitrogen followed by rapid thaw in a 37 °C water bath. Cell debris was pelleted and media was adjusted with a 1:30 dilution of BSA, quick frozen and stored in the −80 °C freezer. RV14 stocks were determined by a TCID50 assay using confluent HeLa cells in 96-well plates as described above, except that assays were developed after 3 day incubation at 33 °C.

**Nanoparticle Treatments.** Nanoparticles were ultrasonicated for 15 min prior to use. Reactions were performed in 24-well plates (Corning, Thermo Fisher Scientific) containing buffer, nanoparticles, and virus as described in figure legends. OC43 and RV14 experiments were performed in 25 mM Tris-hydrogen chloride (Tris-HCl) pH 7.5 solution, containing 1:100 BSA and 75 mM sodium chloride (NaCl). Controls for experiments included buffer with water as a vehicle control (buffer alone). Nanoceria and silver-modified nanoceria were tested at concentrations indicated in the figure legends. Time zero samples were quantified to determine input virus amount. Reactions were incubated at room temperature for times as described in figure legends, followed by quantification of remaining virus infectivity.

**Statistical Analyses.** Statistical analysis was performed using GraphPad students *t* test. In all figures, \* indicates *P*-value <0.05, \*\* indicates *P*-value <0.01, \*\*\* indicates *P*-value <0.001.

**Physical Model of Virus-Nanomaterial interaction via Electrochemical Impedance Spectroscopy.** Virus analogs were determined based on the relative character of a given test viruses surface. To mimic the character of the two viruses for which *in situ* electrochemical impedance spectra were collected (RV14, rhinovirus and OC43, coronavirus), liposome, and bovine serum albumin (BSA) suspensions were prepared in tris-HCl (pH 7.5). These analogs were chosen to reflect the lipid membrane of OC43 and the dense protein surface of RV14, respectively. BSA was dissolved in tris-HCl to a concentration of 5 mg/mL and stored at 4 °C until use. Liposomes were produced by addition of 2 mL tris-HCl to the dry lipid powder. From here, the solution was ultrasonicated using a horn ultrasonicator under 2 min of ultrasonication with an on/off pulse time of 2 s on and 1 s off in an ice-bath to maintain the suspension temperature. Liposomes were stored at 4 °C until use and discarded after 1 week postsynthesis. Size characterization of the liposomes was performed via zeta-sizer measurement (Zeta-sizer Nano, Malvern Instruments). In each test case, the virus-analog material was dispersed in solution and dropcast to the surface of a glassy carbon electrode. Dropcast suspensions were then left to dry under a gentle stream of nitrogen as a film. From here, the modified electrode was then dipped in three washes of dH<sub>2</sub>O to remove any weakly bound particles. Testing was performed under the same conditions (electrolyte volume and composition; AgCNP concentrations; incubation times; electrochemical impedance spectroscopy parameters) as those of the *in situ* measurements with virus species. Experiments for each of the BSA and liposome modified electrode systems were performed with acetaldehyde and xanthine oxidase as a positive control for the generation and influence of free radicals. These measurements were intended to represent any oxidation of the virus analog materials for comparison against the spectra obtained with the AgCNP samples. Before measurement, the activity of stock xanthine oxidase enzyme were first measured and determined such that a concentration of 4.3 units/mL was produced. Ten μL of the enzyme suspension and 10 μL of a 99% acetaldehyde stock solution were added to 3 mL of tris-HCl buffer solution for model studies with electrochemical impedance spectra collected.

## ASSOCIATED CONTENT

### Supporting Information

The Supporting Information is available free of charge at <https://pubs.acs.org/doi/10.1021/acsnano.1c04142>.

Additional materials characterization data, electrochemical control measurements, and discussion. Figure S1

details important material/chemical properties considered by the authors in producing the formulations presented in the manuscript; Figure S2–S6 provide additional materials characterization and analysis with respect to the silver-modified cerium oxide nano material formulations (oxygen xps spectra, silver xps spectrum, additional TEM images, Tauc analysis, and UPS measurements, respectively); Figure S7 shows time-dependent changes in virus titer for both RV14 and OC43 upon two separate, consecutive inoculations; and Figures S8–S16 provide additional data related to electrochemical measurements of (model) virus interactions (PDF)

## AUTHOR INFORMATION

### Corresponding Author

Sudipta Seal – Department of Materials Science & Engineering, Advanced Materials Processing and Analysis Center (AMPAC), Nanoscience Technology Center (NSTC), University of Central Florida, Orlando, Florida 32816, United States; Biionix Cluster, College of Medicine, University of Central Florida, Orlando, Florida 32827, United States; [orcid.org/0000-0002-0963-3344](https://orcid.org/0000-0002-0963-3344); Email: [sudipta.seal@ucf.edu](mailto:sudipta.seal@ucf.edu)

### Authors

Craig J. Neal – Department of Materials Science & Engineering, Advanced Materials Processing and Analysis Center (AMPAC), Nanoscience Technology Center (NSTC), University of Central Florida, Orlando, Florida 32816, United States

Candace R. Fox – Burnett School of Biomedical Sciences, College of Medicine, University of Central Florida, Orlando, Florida 32827, United States

Tamil Selvan Sakthivel – Department of Materials Science & Engineering, Advanced Materials Processing and Analysis Center (AMPAC), Nanoscience Technology Center (NSTC), University of Central Florida, Orlando, Florida 32816, United States

Udit Kumar – Department of Materials Science & Engineering, Advanced Materials Processing and Analysis Center (AMPAC), Nanoscience Technology Center (NSTC), University of Central Florida, Orlando, Florida 32816, United States

Yifei Fu – Department of Materials Science & Engineering, Advanced Materials Processing and Analysis Center (AMPAC), Nanoscience Technology Center (NSTC), University of Central Florida, Orlando, Florida 32816, United States

Christina Drake – Kismet Technologies, Orlando, Florida 32792, United States

Griffith D. Parks – Burnett School of Biomedical Sciences, College of Medicine, University of Central Florida, Orlando, Florida 32827, United States

Complete contact information is available at: <https://pubs.acs.org/10.1021/acsnano.1c04142>

### Author Contributions

All authors contributed to the writing and editing of the manuscript. All authors approve of the submitted version of the manuscript.

## Notes

The authors declare the following competing financial interest(s): C.D. discloses a competing interest as the Founder of Kismet Technologies that has commercialization rights to a pending patent.

## ACKNOWLEDGMENTS

We acknowledge funding from Kismet Tech (through NSF STTR Phase I: IIP: 2032056), Florida High Tech Corridor, and XPS User facility: NSF MRI: ECCS: 1726636. Additionally, we acknowledge the insights and considerations of Dr. M. Molinari (University of Huddersfield, UK); especially with respect to materials characterization. R. Dickerson (UCF, College of Medicine) is also acknowledged for help in artistic conceptualization. Some figures were created in part using BioRender.com.

## REFERENCES

- (1) Walls, A. C.; Park, Y.-J.; Tortorici, M. A.; Wall, A.; McGuire, A. T.; Veesler, D. Structure, Function, and Antigenicity of the SARS-CoV-2 Spike Glycoprotein. *Cell* **2020**, *181*, 281–292. e6.
- (2) Walls, A. C.; Xiong, X.; Park, Y.-J.; Tortorici, M. A.; Snijder, J.; Quispe, J.; Cameron, E.; Gopal, R.; Dai, M.; Lanzavecchia, A. Unexpected Receptor Functional Mimicry Elucidates Activation of Coronavirus Fusion. *Cell* **2019**, *176*, 1026–1039. e15.
- (3) Baker, A. N.; Richards, S.-J.; Guy, C. S.; Congdon, T. R.; Hasan, M.; Zwetsloot, A. J.; Gallo, A.; Lewandowski, J. R.; Stansfeld, P. J.; Straube, A. The Sars-Cov-2 Spike Protein Binds Sialic Acids and Enables Rapid Detection in a Lateral Flow Point of Care Diagnostic Device. *ACS Cent. Sci.* **2020**, *6*, 2046–2052.
- (4) Grant, O. C.; Montgomery, D.; Ito, K.; Woods, R. J. Analysis of the SARS-CoV-2 Spike Protein Glycan Shield Reveals Implications for Immune Recognition. *Sci. Rep.* **2020**, *10*, 1–11.
- (5) Casalino, L.; Gaieb, Z.; Dommer, A. C.; Harbison, A. M.; Fogarty, C. A.; Barros, E. P.; Taylor, B. C.; Fadda, E.; Amaro, R. E. Shielding and Beyond: The Roles of Glycans in SARS-CoV-2 Spike Protein. 2020, bioRxiv. DOI: 10.1101/2020.06.11.146522 (accessed 2021/7/21).
- (6) Watanabe, Y.; Allen, J. D.; Wrapp, D.; McLellan, J. S.; Crispin, M. Site-Specific Analysis of the SARS-CoV-2 Glycan Shield. 2020, bioRxiv. DOI: 10.1101/2020.03.26.010322 (accessed 2021/7/21).
- (7) Theuretzbacher, U. Global Antibacterial Resistance: The Never-Ending Story. *J. Glob. Antimicrob. Resist.* **2013**, *1*, 63–69.
- (8) Levy, S. B.; Marshall, B. Antibacterial Resistance Worldwide: Causes, Challenges and Responses. *Nat. Med.* **2004**, *10*, S122–S129.
- (9) Xiang, D.-x.; Chen, Q.; Pang, L.; Zheng, C.-l. Inhibitory Effects of Silver Nanoparticles on H1N1 Influenza A Virus *In Vitro*. *J. Virol. Methods* **2011**, *178*, 137–142.
- (10) Galdiero, S.; Falanga, A.; Vitiello, M.; Cantisani, M.; Marra, V.; Galdiero, M. Silver Nanoparticles As Potential Antiviral Agents. *Molecules* **2011**, *16*, 8894–8918.
- (11) Gaikwad, S.; Ingle, A.; Gade, A.; Rai, M.; Falanga, A.; Incoronato, N.; Russo, L.; Galdiero, S.; Galdiero, M. Antiviral Activity of Mycosynthetized Silver Nanoparticles against Herpes Simplex Virus and Human Parainfluenza Virus Type 3. *Int. J. Nanomed.* **2013**, *8*, 4303.
- (12) Xiu, Z.-m.; Zhang, Q.-b.; Puppala, H. L.; Colvin, V. L.; Alvarez, P. J. Negligible Particle-Specific Antibacterial Activity of Silver Nanoparticles. *Nano Lett.* **2012**, *12*, 4271–4275.
- (13) Peretyazhko, T. S.; Zhang, Q.; Colvin, V. L. Size-Controlled Dissolution of Silver Nanoparticles at Neutral and Acidic pH Conditions: Kinetics and Size Changes. *Environ. Sci. Technol.* **2014**, *48*, 11954–11961.
- (14) Celardo, I.; Pedersen, J. Z.; Traversa, E.; Ghibelli, L. Pharmacological Potential of Cerium Oxide Nanoparticles. *Nanoscale* **2011**, *3*, 1411–1420.
- (15) Pirmohamed, T.; Dowding, J. M.; Singh, S.; Wasserman, B.; Heckert, E.; Karakoti, A. S.; King, J. E.; Seal, S.; Self, W. T. Nanoceria Exhibit Redox State-Dependent Catalase Mimetic Activity. *Chem. Commun.* **2010**, *46*, 2736–2738.
- (16) Korsvik, C.; Patil, S.; Seal, S.; Self, W. T. Superoxide Dismutase Mimetic Properties Exhibited by Vacancy Engineered Ceria Nanoparticles. *Chem. Commun.* **2007**, *10*, 1056–1058.
- (17) Silva, G. A. Seeing the Benefits of Ceria. *Nat. Nanotechnol.* **2006**, *1*, 92–94.
- (18) Popov, A. L.; Shcherbakov, A. B.; Zholobak, N.; Baranchikov, A. Y.; Ivanov, V. K. Cerium Dioxide Nanoparticles As Third-Generation Enzymes (Nanozymes). *Nanosystems: Phys. Chem. Math.* **2017**, *8*, 760
- (19) Tang, S.; Zheng, J. Antibacterial Activity of Silver Nanoparticles: Structural Effects. *Adv. Healthcare Mater.* **2018**, *7*, 1701503.
- (20) Martínez-Castañón, G.-A.; Nino-Martinez, N.; Martinez-Gutierrez, F.; Martinez-Mendoza, J.; Ruiz, F. Synthesis and Antibacterial Activity of Silver Nanoparticles with Different Sizes. *J. Nanopart. Res.* **2008**, *10*, 1343–1348.
- (21) Lok, C.-N.; Ho, C.-M.; Chen, R.; He, Q.-Y.; Yu, W.-Y.; Sun, H.; Tam, P. K.-H.; Chiu, J.-F.; Che, C.-M. Silver Nanoparticles: Partial Oxidation and Antibacterial Activities. *JBIC, J. Biol. Inorg. Chem.* **2007**, *12*, 527–534.
- (22) Panáček, A.; Kvitek, L.; Prucek, R.; Kolář, M.; Večřová, R.; Pizúrová, N.; Sharma, V. K.; Nevěčná, T. J.; Zbořil, R. Silver Colloid Nanoparticles: Synthesis, Characterization, and Their Antibacterial Activity. *J. Phys. Chem. B* **2006**, *110*, 16248–16253.
- (23) Chen, A.; Yu, X.; Zhou, Y.; Miao, S.; Li, Y.; Kuld, S.; Sehested, J.; Liu, J.; Aoki, T.; Hong, S. Structure of the Catalytically Active Copper–Ceria Interfacial Perimeter. *Nat. Catal.* **2019**, *2*, 334–341.
- (24) Dvořák, F.; Camellone, M. F.; Tovt, A.; Tran, N.-D.; Negreiros, F. R.; Vorokhta, M.; Skála, T.; Matolínová, I.; Mysliveček, J.; Matolín, V. Creating Single-Atom Pt-Ceria Catalysts by Surface Step Decoration. *Nat. Commun.* **2016**, *7*, 1–8.
- (25) Doshi, M.; Bosak, A.; Neal, C. J.; Isis, N.; Kumar, U.; Jeyaranjan, A.; Sakthivel, T. S.; Singh, S.; Willenberg, A.; Hines, R. B.; Seal, S.; Willenburg, B. J. Exposure to Nanoceria Impacts Larval Survival, Life History Traits and Fecundity of *Aedes aegypti*. *PLoS Neglected Trop. Dis.* **2020**, *14*, e0008654.
- (26) Tsai, D.-S.; Yang, T.-S.; Huang, Y.-S.; Peng, P.-W.; Ou, K.-L. Disinfection Effects of Undoped and Silver-Doped Ceria Powders of Nanometer Crystallite Size. *Int. J. Nanomed.* **2016**, *11*, 2531.
- (27) Zhang, F.; Jin, Q.; Chan, S.-W. Ceria Nanoparticles: Size, Size Distribution, and Shape. *J. Appl. Phys.* **2004**, *95*, 4319–4326.
- (28) Symington, A. R.; Molinari, M.; Moxon, S.; Flitcroft, J. M.; Sayle, D. C.; Parker, S. C. Strongly Bound Surface Water Affects the Shape Evolution of Cerium Oxide Nanoparticles. *J. Phys. Chem. C* **2020**, *124*, 3577–3588.
- (29) Gupta, A.; Sakthivel, T. S.; Neal, C. J.; Koul, S.; Singh, S.; Kushima, A.; Seal, S. Antioxidant Properties of ALD Grown Nanoceria Films with Tunable Valency. *Biomater. Sci.* **2019**, *7*, 3051–3061.
- (30) Seal, S.; Jeyaranjan, A.; Neal, C. J.; Kumar, U.; Sakthivel, T. S.; Sayle, D. C. Engineered Defects in Cerium Oxides: Tuning Chemical Reactivity for Biomedical, Environmental, & Energy Applications. *Nanoscale* **2020**, *12*, 6879–6899.
- (31) Murugadoss, G.; Kumar, D. D.; Kumar, M. R.; Venkatesh, N.; Sakthivel, P. Silver Decorated CeO<sub>2</sub> Nanoparticles for Rapid Photocatalytic Degradation of Textile Rose Bengal Dye. *Sci. Rep.* **2021**, *11*, 1080.
- (32) Patil, S. S.; Mali, M. G.; Tamboli, M. S.; Patil, D. R.; Kulkarni, M. V.; Yoon, H.; Kim, H.; Al-Deyab, S. S.; Yoon, S. S.; Kolekar, S. S. Green Approach for Hierarchical Nanostructured Ag-ZnO and Their Photocatalytic Performance under Sunlight. *Catal. Today* **2016**, *260*, 126–134.
- (33) Ivanova, T. V.; Homola, T.; Bryukvin, A.; Cameron, D. C. Catalytic Performance of Ag<sub>2</sub>O and Ag Doped CeO<sub>2</sub> Prepared by Atomic Layer Deposition for Diesel Soot Oxidation. *Coatings* **2018**, *8*, 237.
- (34) Ascarelli, P.; Cini, M.; Missoni, G.; Nistico, N. XPS Line Broadening in Small Metal Particles. *J. Phys. Colloq.* **1977**, *38* (C2), C2–125–C2–128.

- (35) Luches, P.; Pagliuca, F.; Valeri, S.; Illas, F.; Preda, G.; Pacchioni, G. Nature of Ag Islands and Nanoparticles on the CeO<sub>2</sub> (111) Surface. *J. Phys. Chem. C* **2012**, *116*, 1122–1132.
- (36) Preda, G.; Pacchioni, G. Formation of Oxygen Active Species in Ag-Modified CeO<sub>2</sub> Catalyst for Soot Oxidation: A DFT Study. *Catal. Today* **2011**, *177*, 31–38.
- (37) Matovic, B.; Butulija, S.; Dohcevic-Mitrovic, Z.; Arsic, T. M.; Lukovic, J.; Boskovic, S.; Maletaskic, J. Synthesis, Densification and Characterization of Ag Doped Ceria Nanopowders. *J. Eur. Ceram. Soc.* **2020**, *40*, 1983–1988.
- (38) Aneggi, E.; Llorca, J.; de Leitenburg, C.; Dolcetti, G.; Trovarelli, A. Soot Combustion over Silver-Supported Catalysts. *Appl. Catal., B* **2009**, *91*, 489–498.
- (39) Shapovalov, V.; Metiu, H. Catalysis by Doped Oxides: CO Oxidation by AuxCe<sub>1-x</sub>O<sub>2</sub>. *J. Catal.* **2007**, *245*, 205–214.
- (40) Owen, L.; Shivkumar, M.; Laird, K. The Stability of Model Human Coronaviruses on Textiles in the Environment and during Health Care Laundering. *Msphere* **2021**, *6*, e00316–21.
- (41) Elbrecht, D. H.; Long, C. J.; Hickman, J. J. Transepithelial/Endothelial Electrical Resistance (TEER) Theory and Applications for Microfluidic Body-on-a-Chip Devices. *J. Rare Dis. Res. Treat.* **2016**, *1*, 46.
- (42) Gudivaka, R.; Schoeller, D.; Kushner, R.; Bolt, M. Single- and Multifrequency Models for Bioelectrical Impedance Analysis of Body Water Compartments. *J. Appl. Physiol.* **1999**, *87*, 1087–1096.
- (43) Giaever, I.; Keese, C. R. Micromotion of Mammalian Cells Measured Electrically. *Proc. Natl. Acad. Sci. U. S. A.* **1991**, *88*, 7896–7900.
- (44) Stupin, D. D.; Kuzina, E. A.; Abelit, A. A.; Koniakhin, S. V.; Emelyanov, A. E.; Nikolaev, D. M.; Ryazantsev, M. N.; Dubina, M. V. Bio-Impedance Spectroscopy: Basics and Applications. *ACS Biomater. Sci. Eng.* **2021**, *7*, 1962–1986.
- (45) Grimnes, S.; Martinsen, Ø. G. Alpha-Dispersion in Human Tissue. *J. Phys.: Conf. Ser.* **2010**, *224*, 012073.
- (46) Jacobs, S.; Lamson, D.; George, K., St.; Walsh, T. J. Human Rhinoviruses. *Clin. Microbiol. Rev.* **2013**, *26*, 135–162.
- (47) Johnson, J. B.; Lyles, D. S.; Alexander-Miller, M. A.; Parks, G. D. Virion-Associated Complement Regulator CD55 Is More Potent than CD46 in Mediating Resistance of Mumps Virus and Vesicular Stomatitis Virus to Neutralization. *J. Virol.* **2012**, *86*, 9929–9940.
- (48) Hierholzer, J.; Killington, R. Virus Isolation and Quantitation. In *Virology Methods Manual*; Mahy, B., Kangro, H., Eds.; Elsevier, 1996; pp 25–46.
- (49) Bracci, N.; Pan, H.-C.; Lehman, C.; Kehn-Hall, K.; Lin, S.-C. Improved Plaque Assay for Human Coronaviruses 229E and OC43. *PeerJ* **2020**, *8*, e10639.